

# Effects of Al Precursors on the Characteristics of Indium–Aluminum Oxide Semiconductor Grown by Plasma-Enhanced Atomic Layer Deposition

Seunghee Lee, Miso Kim, Geumbi Mun, Jongbeom Ko, Hye-In Yeom, Gwang-Heum Lee, Bonggeun Shong,\* and Sang-Hee Ko Park\*



Cite This: <https://doi.org/10.1021/acsami.1c11304>



Read Online

ACCESS |



Metrics & More



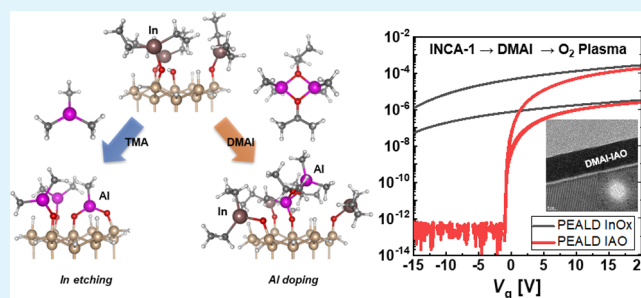
Article Recommendations



Supporting Information

**ABSTRACT:** Atomic layer deposition (ALD) has attracted much attention, particularly for applications in nanoelectronics because of its atomic-level controllability and high-quality products. In this study, we developed a plasma-enhanced atomic layer deposition (PEALD) process to fabricate a homogeneous indium aluminum oxide (IAO) semiconductor film. Trimethylaluminum (TMA) and dimethylaluminum isopropoxide (DMAI) were used as Al precursors, which yielded different compositions. Density functional theory (DFT) calculations on the surface reactions between indium and aluminum precursors showed that while highly reactive TMA would etch In, DMAI with lower reactivity would allow indium to persist in the films, resulting in a more controlled doping of Al. The In/Al composition ratio could be further precisely controlled by adjusting the indium precursor dose time to sub-saturation. IAO based on DMAI was applied to fabricate thin-film transistors (TFTs), showing that Al can be a carrier suppressor of indium oxide. TFTs with PEALD IAO containing 3.8 atomic % Al showed a turn-on voltage of  $-0.4 \pm 0.3$  V, a subthreshold slope of 0.09 V/decade, and a field effect mobility of  $18.9 \text{ cm}^2/(\text{V s})$ .

**KEYWORDS:** *InAlO*, multicomponent ALD, surface chemistry, dimethylaluminum isopropoxide, trimethylaluminum, TFT



## INTRODUCTION

Oxide semiconductors have been actively studied for active matrix flat-panel displays owing to their remarkable characteristics such as high mobility, low leakage current, large-area uniformity, and transparency.<sup>1,2</sup> Recently, the demand for ultrahigh-resolution displays is increasing rapidly with interest in virtual reality, augmented reality, and micro-light-emitting diode (micro-LED) displays. Thus, a three-dimensional (3D) structure is required for scaled-down thin-film transistors (TFTs). The sputtering method is inadequate for uniform deposition of oxide semiconductor on fine 3D structures.<sup>3</sup> To solve this problem, many studies have been carried out to investigate the deposition of oxide semiconductors using the atomic layer deposition (ALD) method, which produces excellent step coverage and uniformity by controlling the layer down to the angstrom scale through a surface-limited reaction.<sup>4–6</sup>

Among the oxide semiconductors, indium oxide ( $\text{InO}_x$ ) is well known to have high carrier density and high mobility. The high carrier density of  $\text{InO}_x$  results from both the oxygen vacancies generated by weak bond energy between In and O and corner sharing of vacancy in the crystalline phase.<sup>7,8</sup> Oxygen vacancies ( $V_{\text{O}}$ ) significantly affect the electrical properties of oxide semiconductors since they can behave as shallow donors

and trap sites. Therefore, it is difficult to control the performance of indium oxide TFT in terms of the threshold voltage and bias stability.<sup>9</sup> Thus, the modification of chemical composition is necessary for improvement of the electrical performance of the indium oxide-based TFTs.<sup>10</sup>

Indium-based multication systems have been applied to induce strong metal–oxygen binding by decreasing oxygen vacancy defects and deterring crystallization.<sup>11–13</sup> Among possible dopant elements, Al has a large bond dissociation energy with oxygen (502 kJ/mol), larger than that of Ga (374 kJ/mol), and is abundant in Earth's crust.<sup>7,14</sup> Several studies have verified the performance of Al-doped oxide semiconductors such as sputtered Al:In–Sn–Zn–O,<sup>15</sup> Al–In–Zn–O,<sup>14,16,17</sup> and solution-processed In–Al–O (IAO) films.<sup>18</sup> However, Al doping in  $\text{InO}_x$  through plasma-enhanced atomic layer deposition (PEALD) has not yet been demonstrated.

Received: June 17, 2021

Accepted: August 2, 2021

As the ALD is carried out by sequential pulsing of the metal precursor and reactant, it can yield binary, ternary, and quaternary thin films through varied gas sequences. Previously reported ALD oxide semiconductor TFTs such as In–Ga–Zn–O (IGZO),<sup>19,20</sup> In–Ga–O (IGO),<sup>21</sup> In–Zn–O (IZO),<sup>4</sup> and In–Zn–Sn–O (IZTO)<sup>22</sup> were often deposited using supercycle method. The supercycle (AO → BO) method produced ternary oxide films by repeating each binary oxide cycle.<sup>23</sup> For doping of an element with relatively low concentration, a single cycle of the dopant layer is applied between thick layers of the host oxide layer, so that the film often exhibits different doping densities in the lateral and vertical directions.<sup>24</sup> The thick interlayer works as a vertical diffusion barrier that interrupts the intermixing. Therefore, it was responsible for the poor on–off characteristics of TFTs over a vertical dimension of 3.5 nm.<sup>19</sup> Hence, other approaches, in which two different metal precursors are converted into ternary oxide films during a single cycle, have been proposed.<sup>23</sup> The first method is to use a multiconstituent precursor with multiple metal centers (AB → O). However, it is difficult to develop new precursors suitable for ALD. Furthermore, as the composition is determined by the molecular reactivity of the single precursor, such approach is limited in the arbitrary adjustment of the composition.<sup>25</sup> The second is the co-dosing method (A + B → O) by pulsing two precursors together. As the growth of film relies on the competitive adsorption of the two precursors depending on their amount and reactivity, the uniform coating characteristics of the complex structure might be potentially deteriorated.<sup>23</sup> The last is the multistep method (A → B → O) in which the precursors are sequentially injected into the reaction chamber.<sup>26,27</sup> In this method, the film growth is governed by the coverage of the first precursor, as well as on-surface mixing of the second precursor, enabling reproducible uniform formation of multicomponent thin films.<sup>23</sup>

To uniformly distribute the dopant in the thin films, it is necessary to control the surface reaction of each precursor. However, in the case of the Al-doped multicomponent ALD process of Al–Zn–O using trimethylaluminum (TMA) and diethylzinc (DEZ), the TMA exposure resulted in negative growth (loss of mass).<sup>28,29</sup> The TMA precursor is well-known to possess extremely high reactivity toward ligand-exchange reactions, so that the lattice atoms of the surface are often removed as volatile reaction products that leads to etching of the substrate.<sup>30–32</sup> Therefore, an alternative Al precursor is essential. For area-selective atomic layer deposition (AS-ALD) of Al<sub>2</sub>O<sub>3</sub>, dimethylaluminum isopropoxide (DMAI) was proposed as an alternative precursor that increase the deposition selectivity, since it is better blocked by the pre-adsorbed surface inhibitors than TMA.<sup>33</sup>

In this study, we fabricated In–Al–O (IAO) films using the PEALD and controlled the composition of indium and aluminum by a multistep sequence (A → B → O) for the application to the TFT. The indium precursor for In<sub>2</sub>O<sub>3</sub> film deposition was bis(trimethylsilyl)amidodiethylindium (INCA-1). For the successful incorporation of Al into the InO<sub>x</sub> film, we adopted DMAI as an Al precursor, whose results are compared to those of TMA. Density functional theory (DFT) calculations were executed to scrutinize the interaction between precursors. As a result, Al doping of indium oxide with DMAI was successful without etching of In. In the multistep method, the Al doping concentration was regulated by unsaturated dose time of INCA-1 because unsaturated surface left reactive area for the subsequent chemisorption of DMAI. To verify the doping effect of Al in indium oxide semiconductor, we analyzed the

chemical, crystalline, optical, and electrical properties. We confirmed that Al doping in InO<sub>x</sub> via PEALD successfully contained a reduced number of oxygen vacancy defects and an amorphous phase. Finally, ALD-IAO films were applied to bottom-gate–bottom-contact (BGBC) TFT to yield improved on/off characteristics and stability. The electrical properties of IAO TFTs were successfully controlled; these devices showed a turn-on voltage of  $-0.4 \pm 0.3$  V and a high mobility of 18.9 cm<sup>2</sup>/ (V s).

## METHODS

**ALD Processes.** We deposited indium oxide and aluminum oxide films on Si(100) wafer and glass substrates utilizing a showerhead type PEALD system (Atomic-Premium, CN1, Co., Ltd., Korea) at 250 °C. Si substrates were cleaned by BOE 6:1. Si and glass substrates were exposed to O<sub>2</sub> plasma prior to deposition in vacuum. InO<sub>x</sub>, Al<sub>2</sub>O<sub>3</sub>, and IAO films were deposited at a thickness of ~15 nm. INCA-1, (99.99%, UP Chem, Co., Ltd.) and DMAI (99.99%, DNF, Co., Ltd.) were stored in a bubbler-type canister at 40 and 50 °C, respectively. TMA (99.9999%, UP Chem Co., Ltd.) was held at room temperature. The precursors were used without further purification. The O<sub>2</sub> plasma reactant was generated in situ with O<sub>2</sub> gas (99.999%) and a radio frequency (RF) plasma power of 100 W. O<sub>2</sub> plasma (500 sccm) was applied for 2 s to all the PEALD processes. Ar gas (99.999%) was used as the purge gas (1000 sccm) and carry gas (50 sccm) of bubbler-type canisters. Pressure was maintained at 1–1.1 Torr. The ALD sequence time for PEALD-InO<sub>x</sub> was 1.4–40–2–30 s. PE-Al<sub>2</sub>O<sub>3</sub> (TMA) was optimized with TMA 0.1 s–Ar 10 s–O<sub>2</sub> plasma 2 s–Ar 7 s and PE-Al<sub>2</sub>O<sub>3</sub> (DMAI) was deposited with DMAI 0.1 s–Ar 15 s–O<sub>2</sub> plasma 2 s–Ar 15 s. Table S1 shows the details of the ALD recipes and cycles in case 1, case 2, case 3, and case 4 for IAO-1 and IAO-2 films.

**Characterization of Films.** The thickness and refractive index of each film were obtained using an ellipsometer (Alpha-SE, J.A. Woollam Co.). The densities of the films were measured using the X-ray reflectometry (XRR, SmartLab, Rigaku Corp.) technique and fitting program. X-ray photoelectron spectroscopy (XPS, K-Alpha XPS system, Thermo Fisher Scientific, Inc.) was used to analyze the chemical composition of the films. The optical transmittance was obtained using a UV–vis–NIR spectrophotometer (SolidSpec-3700, Shimadzu Co. Ltd.), and the imaginary part of the dielectric function was obtained from a spectroscopic ellipsometer (M2000D, J.A. Woollam Co., Inc.) data. The crystal structures of the films were analyzed by X-ray diffraction (XRD, Ultima IV, Rigaku Corp.) and field emission scanning transmission electron microscopy (FE-STEM, HD-2300A, Hitachi Co., Ltd.). Hall effect measurements of the oxide semiconductor films were performed using an ACCENT HL5500 Hall system at room temperature.

**DFT Calculations.** DFT calculations were carried out using Gaussian 16 program<sup>34</sup> with the dispersion-corrected B97-D3 functional<sup>35</sup> and def2-SVP basis set.<sup>36</sup> The Gibbs free energy (*G*) of dimerization of the precursors were obtained at 250 °C and 1 Torr, following the equation

$$G = H - TS \quad (1)$$

To model the substrate surface, a Si<sub>26</sub>H<sub>26</sub> cluster that resembles the Si(111) surface was constructed.<sup>40</sup> The occupation of the central (c) and surrounding (s) surface sites were set to simulate different functionalization conditions; that is, (i) c = OH and s = OInEt<sub>2</sub>, (ii) c and s = OInEt<sub>2</sub>, and (iii) c = OIn(OH)<sub>2</sub> and s = OH. The geometries of the transition states were confirmed after optimization by having an imaginary vibrational mode along the reaction coordinate. All reported energy values for the surface reactions are calculated at 0 K and do not include zero-point energy correction.

**Fabrication of TFT Devices and Analysis of Electrical Properties.** TFTs with bottom-gate–bottom-contact (BGBC) structure were fabricated on indium tin oxide (ITO) glass (Geomatec Co., Ltd.). The 150 nm ITO gate electrode was patterned using photolithography. A 165 nm thick Al<sub>2</sub>O<sub>3</sub> film was deposited as a gate insulator at 150 °C by thermal ALD. A sputtered ITO film (150 nm)

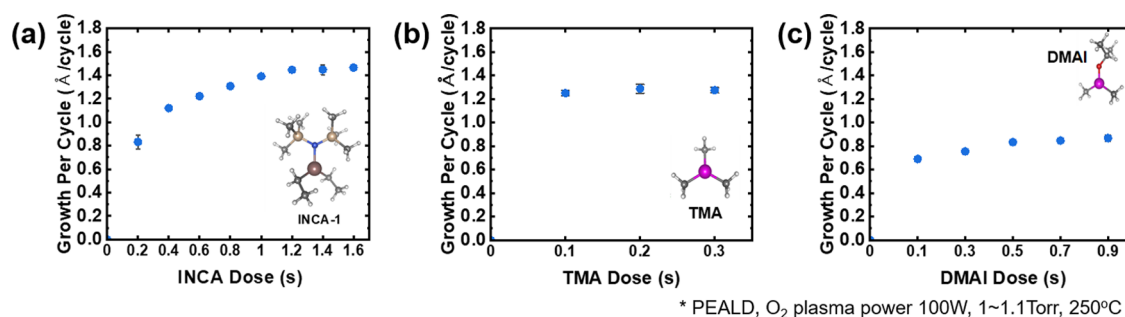


**Figure 1.** Growth per cycle of PEALD: (a) indium oxide as a function of the INCA-1 dose, (b) aluminum oxide using TMA, and (c) aluminum oxide using DMAI (insets: molecular structures of metal precursors used in PEALD. Brown = In, purple = Al, yellow = Si, red = O, blue = N, gray = C, white = H).

**Table 1. Summary of PEALD Binary Oxide Films Characteristics: Thickness, Refractive Index, Film Density, GPC, and Area Density Per Cycle**

film	thickness (nm)	cycle	refractive index	density (g/cm <sup>3</sup> )	GPC (Å/cycle)	area density per cycle <sup>a</sup> (ng/(cm <sup>2</sup> cycle))
InO <sub>x</sub>	13.00	90	1.89	5.91	1.40	8.274
Al <sub>2</sub> O <sub>3</sub> (TMA)	14.95	125	1.69	3.61	1.19	4.041
Al <sub>2</sub> O <sub>3</sub> (DMAI)	12.83	160	1.67	3.12	0.80	2.496

<sup>a</sup>Area density per cycle = density × GPC.

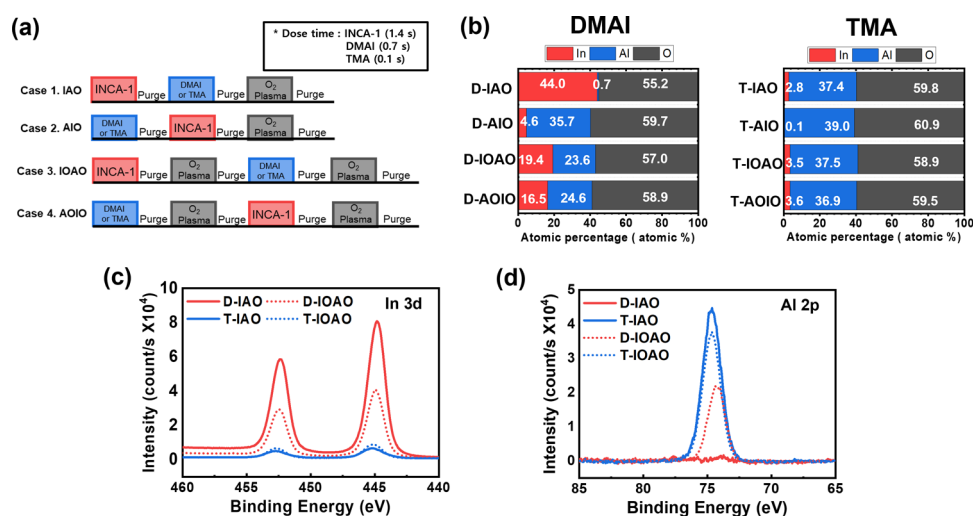


**Figure 2.** (a) Schemes of various ALD sequences of indium aluminum oxide film. (b) Atomic percentages of indium (red bar), aluminum (blue bar), and oxygen (black bar) according to the aluminum precursor in each ALD sequence. (c, d) XPS spectra of D-IAO (red solid), T-IAO (blue solid), D-IOAO (red dot), and T-IOAO (blue dot) films: (c) In 3d peaks and (d) Al 2p peaks.

was deposited as the source/drain electrode, followed by annealing at 250 °C under vacuum. After the source/drain electrode patterning by wet etching, the InO<sub>x</sub> and IAO films were grown by PEALD as active layers. After O<sub>2</sub> annealing at 350 °C for 2 h, a 100 nm thick SiO<sub>2</sub> film was deposited as a passivation layer using plasma-enhanced chemical vapor deposition (PECVD) at 300 °C. Finally, the fabricated TFTs were post-annealed at 300 °C for 2 h under vacuum.

For the electrical analysis of the TFTs, a semiconductor parameter analyzer (HP 4156, Agilent Technologies) and a probe station were used. The transfer curve of the BGBC TFT, which was applied to the gate voltage ( $V_G = -15$  to 20 V) and the drain voltage ( $V_D = 0.1, 10$  V) was measured with a channel width of 40  $\mu\text{m}$  and length of 20  $\mu\text{m}$ . The electrical characteristics of the device were averaged from 12ea devices on the same substrate. The bias stability of TFTs under positive bias stress (PBS) and negative bias stress (NBS) were evaluated in ambient air, under a gate bias field of  $\pm 1$  MV/cm for a total stress time of 10 000 s. The illumination stability of the device was measured under NBS by applying a gate bias field of 1 MV/cm and an illumination power of 0.5

mW for 10 000 s. The reliability of the measurements was evaluated by analyzing the devices having the most similar characteristics.

## RESULTS AND DISCUSSION

**Precursor-Dependent Surface Chemistry in PEALD of IAO.** To examine the film growth behavior with respect to the precursor dose time, we deposited the indium oxide and aluminum oxide films using the corresponding precursors on a Si(100) substrate at 250 °C, as shown in Figure 1a–c. The growth per cycle (GPC) of each layer was measured by spectroscopic ellipsometry (SE). The growth rate of the indium oxide film saturated at  $\sim 1.4$  Å/cycle after a pulsing time of 1.2 s. TMA with high vapor pressure resulted in fast saturation within 0.1 s and had a GPC of  $\sim 1.2$  Å/cycle. The surface-limited reaction of DMAI was observed after 0.5 s dosing time with GPC of  $\sim 0.8$  Å/cycle. The GPC of each film was qualitatively similar to those of earlier PEALD studies.<sup>8,37,38</sup> The density and

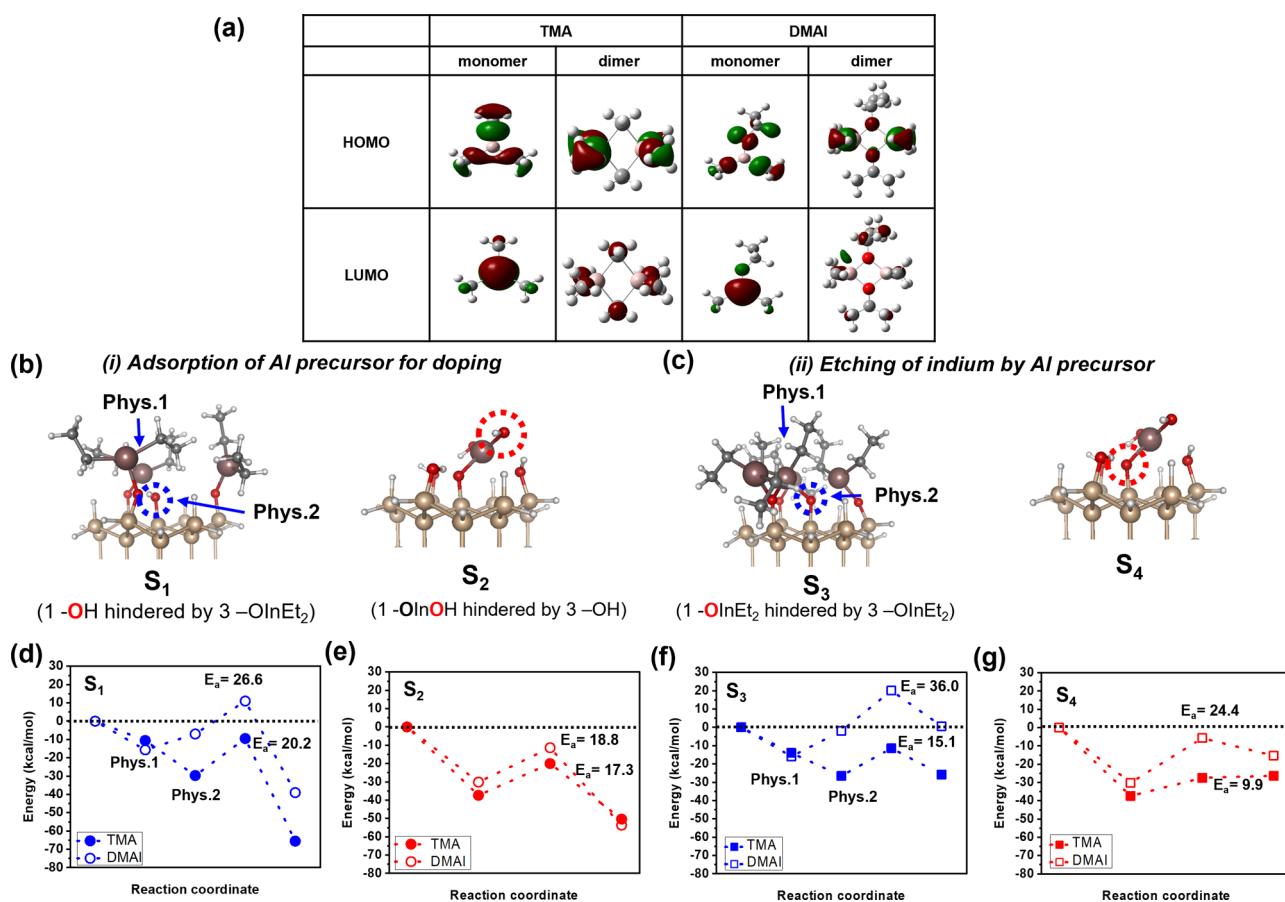


**Figure 3.** (a) Frontier molecular orbitals of Al precursors (isovalue = 0.5). DFT calculation surface models of (b) adsorption of Al precursor for doping (S<sub>1</sub> and S<sub>2</sub>) and (c) etching of the indium compound by the Al precursor (S<sub>3</sub> and S<sub>4</sub>) (brown = In, yellow = Si, red = O, blue = N, gray = C, white = H). Relative energy diagrams on (d) S<sub>1</sub>, (e) S<sub>2</sub>, (f) S<sub>3</sub>, and (g) S<sub>4</sub> according to Al precursors.

thickness of the thin films were analyzed with XRR (Figure S1, Supporting Information), and the values are shown in Table 1. The film densities of InO<sub>x</sub>, Al<sub>2</sub>O<sub>3</sub>(TMA), and Al<sub>2</sub>O<sub>3</sub>(DMAI) were approximately 5.91, 3.61, and 3.12 g/cm<sup>3</sup>, respectively. The area density per cycle was calculated by multiplying the GPC with the density. DMAI had a relatively low area density per cycle, at approximately 2.496 ng/cm<sup>2</sup> cycle, in comparison with TMA of 4.041 ng/cm<sup>2</sup> cycle. The number of Al atoms per cycle in Al<sub>2</sub>O<sub>3</sub> from DMAI was ca. 61% of that from TMA. The refractive indices of Al<sub>2</sub>O<sub>3</sub> films grown with TMA and DMAI were 1.69 and 1.67, respectively, as measured by ellipsometry at 632 nm.<sup>38</sup> To assess the chemical properties of the Al<sub>2</sub>O<sub>3</sub> and In<sub>2</sub>O<sub>3</sub> films deposited by PEALD, XPS studies were conducted, as illustrated in Figure S2, Supporting Information. The effect of surface contamination was eliminated by surface Ar sputtering for 30 s. The binding energies of the In 3d, Al 2p, O 1s, Si 2p, and C 1s peaks were analyzed. The C 1s peaks were not observed in the Al<sub>2</sub>O<sub>3</sub> and InO<sub>x</sub> films. The Al 2p and O 1s peaks of DMAI–Al<sub>2</sub>O<sub>3</sub> appeared at 74.7 and 531.2 eV, respectively. These peaks were similar to those of TMA–Al<sub>2</sub>O<sub>3</sub>. InO<sub>x</sub> films had unintentional incorporation of Si using INCA-1 and O<sub>2</sub> plasma as mentioned in a previous study.<sup>8</sup> The O 1s peak of In<sub>2</sub>O<sub>3</sub> was asymmetrical compared to that of Al<sub>2</sub>O<sub>3</sub> (see Figure S2c, Supporting Information), indicating the presence of multiple states of oxygen in the oxide lattice.<sup>15</sup>

The ALD sequences for deposition of the indium–aluminum oxide thin films are shown in Figure 2a. For multistep approaches, including case 1 of IAO (In–Al–O sequence)

and case 2 of AIO (Al–In–O sequence), two metal precursors were sequentially pulsed, and then oxidized at the same time by the O<sub>2</sub> plasma. The composition of these films was determined by a correlation between a first chemisorbed metal precursor and a subsequent metal precursor. Then, in supercycle approaches of case 3 (IOAO: In–O–Al–O) and case 4 (AOIO: Al–O–I–O), InO<sub>x</sub> and Al<sub>2</sub>O<sub>3</sub> ALD cycles are combined. In such cases, adsorption of TMA and DMAI would occur on the –OIn(OH)<sub>x</sub> surfaces. Here, the dose time of each precursor was set sufficiently to yield a saturated surface reaction: 1.4 s for INCA, 0.7 s for DMAI, and 0.1 s for TMA. Figure 2b shows the atomic percentage (atomic %) of indium, aluminum, and oxygen in the films obtained from the XPS survey peaks (Figure S3, Supporting Information) for each case. The Si peak was excluded from the element ratio extraction to focus on indium and aluminum. In case 1 for IAO, the atomic percentages of In and Al were significantly different depending on the Al precursor. The D-IAO thin film, deposited using DMAI, was mostly InO<sub>x</sub> including only 0.7 atomic % of Al, whereas the T-IAO thin film was mostly composed of Al<sub>2</sub>O<sub>3</sub> with 2.8 atomic % of In. In the IAO ALD sequence, even though the surface was already saturated with INCA-1, the difference of In 3d peak intensity between D-IAO and T-IAO film was large as shown in Figure 2c (solid line). This result indicates that for IAO film (case 1), each Al precursor had a different effect on the adsorbed INCA-1. On the other hand, in case 2 using either DMAI and TMA (D-AIO and T-AIO, respectively), both deposited films

had high Al content, indicating that the impact of INCA-1 on the pre-adsorbed Al precursor would be minor.

For cases 3 and 4, the atomic % of both In and Al were comparable (ca. 16–25%) in the films deposited using DMAI (D-IOAO and D-AOIO). However, both T-IOAO and T-AOIO were formed with only small amounts of In. From this, it could be confirmed that the degree of influence on the composition of each Al precursor is different even when the surface was covered with  $-\text{In}(\text{OH})_x$ . For D-IOAO and T-IOAO, the In 3d and Al 2p peaks are indicated as dotted lines in Figure 2c,d. The Al 2p peak of D-IOAO shifted to a lower binding energy due to the neighboring In atoms. Since the electronegativity of indium was lower than that of oxygen, the electron density around Al increased, resulting in a decrease in the binding energy. Figure S4, Supporting Information, shows refractive indexes of films as a function of the ratio of In and Al. The refractive indexes of  $\text{InO}_x$  and  $\text{Al}_2\text{O}_3$  films were measured by SE. The  $\text{Al}_2\text{O}_3$  has a lower refractive index than that of  $\text{InO}_x$  as shown in Table 1. Accordingly, in indium aluminum oxide films, the decrease of refractive index indicated an increase in the aluminum content. In particular, most of IOAO films using TMA exhibited a refractive index of approximately 1.7, indicating majority of aluminum oxide.

To investigate the precursor-dependent surface chemistry, DFT calculations were conducted. First, we analyzed the dimerization energy and frontier molecular orbital (FMO: highest occupied molecular orbital (HOMO) and lowest unoccupied molecular orbital (LUMO)) of the metal precursors at 250 °C and 1 Torr. The dimerization equation is as follows



The equilibrium constant for dimerization of precursors,  $K$ , is given by

$$K = e^{-(\Delta G/RT)} \quad (3)$$

The Gibbs free energy values for dimerization of  $\text{TMA}_m$ ,  $\text{DMAI}_m$ , and  $\text{INCA-1}_m$  were 40.7,  $-94.5$ , and  $84.4$  kJ/mol, respectively. The dimerization free energy of TMA and INCA were positive, whereas that of DMAI was negative so that DMAI forms a more stable dimer than other two precursors. The equilibrium constant ( $K$ ) values estimated from the DFT-calculated dimerization free energy were  $8.7 \times 10^{-5}$ ,  $3.7 \times 10^{-9}$ , and  $2.7 \times 10^9$  for TMA, INCA-1, and DMAI, respectively. Thus, it can be expected that large fraction of TMA and INCA-1 were in the monomeric form, while DMAI was mostly in the dimeric form under ALD conditions.<sup>38</sup> Figures 3a and S5a, Supporting Information, show the surface of the FMOs of TMA, DMAI, and INCA-1. The LUMO of monomeric precursor was localized on metal atom, while that of dimeric precursors was relatively delocalized. Thus, the monomeric precursor can strongly interact with nucleophilic oxygen on the substrate. Hence, we compared monomeric TMA ( $\text{TMA}_m$ ) with dimeric DMAI ( $\text{DMAI}_d$ ) for the Al-doped indium oxide ALD process.

Figure 3b shows the surface models for adsorption of Al precursor on case 1 ( $S_1$ ) and case 3 ( $S_2$ ). The surface modelings of etching indium compound by Al precursor in case 1 ( $S_3$ ) and case 3 ( $S_4$ ) are illustrated in Figure 3c. Phys.1 was molecular physisorption on  $-\text{InEt}_2$  groups, and Phys.2 was the physisorption on inside  $-\text{OH}$  group.

In case 1 (IAO), INCA-1 was first exposed to the surface, and then followed by exposure to the Al precursor. We designed surface  $S_1$  with one  $-\text{OH}$  group and three  $-\text{InEt}_2$  groups to model the adsorption behavior of the Al precursor after INCA-1

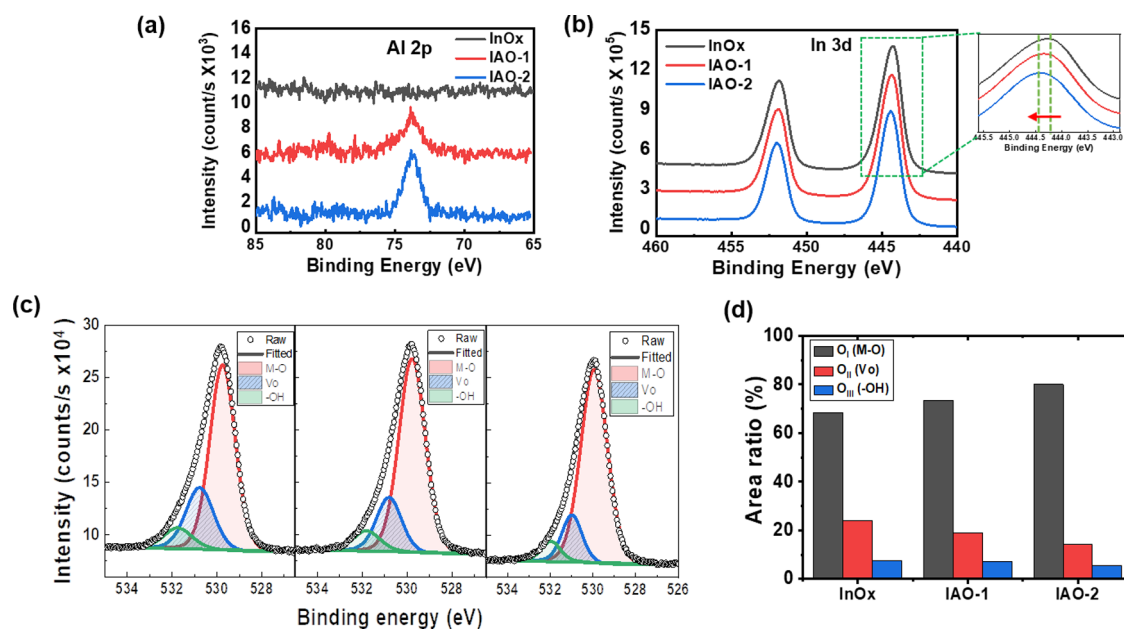
was adsorbed on the surface. Figure 3d shows the reactivity of the Al precursors to the  $S_1$  surface. In the case of molecular adsorption of TMA, Al–O dative bonding was formed spontaneously to  $-\text{OH}$  groups on the surface. The dative bonding TMA with the surface O atoms had similar large adsorption energy in the range of ca.  $-30$  to  $-40$  kcal/mol, regardless of the model configurations. In contrast, for DMAI, while the molecular adsorption energy of on less-hindered  $S_2$  was similar to that of TMA, its adsorption on the In-covered  $S_1$  model was significantly less stable. The reason is that DMAI was relatively large, so it had difficulty in penetrating the  $-\text{InEt}_2$  groups on the surface and binding to the interior  $-\text{OH}$ . In addition, the activation energies ( $E_a$ ) of TMA and DMAI were 20.2 and 26.6 kcal/mol, respectively, for removing methyl ligands via hydrogen transfer from  $-\text{OH}$  groups and leaving Al ions on the surface. Figure S5b shows the adsorption behavior on surface  $S_0$ , where only  $-\text{OH}$  groups existed without the  $-\text{InEt}_2$  groups. When comparing  $S_1$  and  $S_0$ , the  $E_a$  of TMA increased by 3.8 kcal/mol and the  $E_a$  of DMAI increased by 14.8 kcal/mol. After INCA-1 was adsorbed on the surface, the reaction of the Al precursor, especially TMA, with the surface  $-\text{OH}$  became easy due to the small size and high reactivity. The easy nucleation of TMA has been reported even on inhibitor-covered surfaces.<sup>39,40</sup>

Furthermore, since inclusion of TMA in either multistep or supercycle processes resulted in small atomic % of In, etching of In by the Al precursors were considered. We designed the surface model,  $S_3$ , which has four  $-\text{OInEt}_2$  groups, as shown in Figure 3c, and the relative energy diagram is shown in Figure 3f. First, TMA ( $-13.9$  kcal/mol) and DMAI ( $-15.8$  kcal/mol) can be physically adsorbed on the  $-\text{InEt}_2$  groups of the surface (Phys.1). Then, the precursors can move to the oxygen that is part of the  $-\text{OInEt}_2$  group (Phys.2), and the adsorption energies were  $-26.5$  and  $-2.0$  kcal/mol, respectively. To etch indium, the methyl ligand of the Al precursor would migrate to indium and be removed in the form of gaseous  $\text{InEt}_2\text{Me}$ . The removal of a ligand of  $\text{TMA}_m$  via transfer of methyl from the precursor to the indium atom involved an  $E_a$  of 15.1 kcal/mol and an exothermic reaction of  $-25.8$  kcal/mol, while the removal of a ligand of  $\text{DMAI}_d$  via transfer of methyl from the precursor to the indium atom involved an activation barrier of 36.0 kcal/mol and an endothermic reaction of 0.7 kcal/mol. We expect that TMA would have broken the In–O bond, formed an Al–O bond, and released  $\text{InEt}_2\text{Me}$  more easily than DMAI.

In the experimental case 2 of AIO sequence, the Al precursors were first exposed to the substrate surface, on which the INCA-1 precursor was exposed; the film was mostly Al with small fraction of In. Figure S5c (Supporting Information) shows the possible pathways for etching of Al by INCA-1 from the TMA-adsorbed surface ( $S_5$ ) and the DMAI-adsorbed surface ( $S_6$ ), assuming ligand exchange mechanism. The  $E_a$  of INCA-1 on  $S_5$  and  $S_6$  was similar at 24.0 and 26.0 kcal/mol, respectively. However, such reaction is not preferred since the total energy was endothermic. Although such reactions were both unfavorable, the experimentally observed fraction of indium in D-AIO was slightly higher than that of T-AIO, which could be due to the following reason. In the case of TMA, its small molecular size would yield high coverage upon adsorption, consuming most  $-\text{OH}$  groups on the surface, so that adsorption of INCA-1 was effectively hindered. On the other hand, the areal density of relatively bulky DMAI on the substrate would have been sparser, so that some INCA-1 can adsorb on the remaining empty space among chemisorbed DMAI.

**Table 2.** Summary of Thickness, Density, and Atomic Percentage of InO<sub>x</sub> and Multistep PEALD-IAO Films Using INCA-1 and DMAI

film	thickness (nm)	cycle	density (g/cm <sup>3</sup> )	atomic percentage (atomic %)				
				Al	In	O	Si	Al/In
InO <sub>x</sub>	13.00	90	5.91		47.3	50.6	2.1	
IAO-1	12.573	100	5.77	1.1	46.0	51.0	1.9	2.39
IAO-2	12.638	120	5.73	3.8	42.7	51.6	1.7	8.90

**Figure 4.** XPS spectra of InO<sub>x</sub> and IAO films using INCA-1 and DMAI of (a) Al 2p peaks, (b) In 3d peaks, (c) O 1s peaks, and (d) areal ratios of the oxygen deconvolution peaks.

In case 3 of IOAO and case 4 of AOIO, the  $-\text{OH}$  group existed on the surface in both cases, and the next exposed precursor can react with the surface. Figure 3e shows the energy diagram of the possible adsorption reactions of TMA and DMAI with the  $-\text{In}(\text{OH})_2$  group. The  $E_a$  values of TMA and DMAI are similar to 17.3 and 18.8 kcal/mol, respectively (in Figure 3e). The reaction was predicted to be spontaneous because the total reaction energy was exothermic. In addition, the In atoms on the oxidized form would also be etched by TMA, but not by DMAI. Figure 3g shows the reaction energy diagrams of TMA and DMAI with  $-\text{In}(\text{OH})_2$  on the surface, producing  $\text{In}(\text{OH})_2(\text{Me})$  as a possible etch product. The  $E_a$  values of etch processes by TMA and DMAI were 9.9 and 24.4 kcal/mol, respectively, indicating that etching occurs easily when TMA is used. This is consistent with the experimental results. These etching trends are in line with the previous discussion related to ALE. According to ALE using sequential hydrogen fluoride (HF) and TMA, the conversion-etch mechanism can be expected when a metal precursor can form a metal oxide that was more stable than the initial metal oxide.<sup>30</sup>  $\Delta G$  values have been thermodynamically favorable for the reaction between TMA and  $\text{In}_2\text{O}_3$  ( $\text{In}_2\text{O}_3 + 2\text{Al}(\text{CH}_3)_3(\text{g}) = \text{Al}_2\text{O}_3 + 2\text{In}(\text{CH}_3)_3(\text{g})$ ,  $\Delta G = -317.89$  kcal).<sup>30</sup> It has also been reported that In component from organic-inorganic hybrid indicone films can be removed by vacuum annealing, since the In-O binding energy is relatively weak.<sup>41</sup> In summary, TMA would accelerate the etching reaction of In from the substrate because of the small precursor size and high reactivity in the ALD multicomponent deposition. As a result, a multistep IAO thin film using TMA had

formed an insulating film, and hence was not suitable for application as a TFT channel material of TFT. In contrast, DMAI can be used as a carrier control precursor to offer semiconductor characteristics to the films prepared using a multistep ALD sequence ( $A \rightarrow B \rightarrow O$ ) as it does not affect the desorption of host In.

**Homogeneous PEALD-IAO Thin Films and Analysis of the Film Characteristics.** In the showerhead-type ALD, the precursor was evenly sprayed on the substrate and the reactant flux was uniformly distributed, regardless of the reactant dose. Using this advantage, the D-IAO multistep process enabled deposition of homogeneous, uniformly doped ternary oxide films in one cycle. The doping concentration of Al could be further controlled by adjusting sub-saturation dose time of INCA-1. There were three types of homogeneous metal oxide semiconductors that play as active layers in TFTs: InO<sub>x</sub> (INCA-1 for 1.4 s + O<sub>2</sub> plasma), IAO-1 (INCA-1 for 0.8 s + DMAI for 0.7 s + O<sub>2</sub> plasma), and IAO-2 (INCA-1 for 0.4 s + DMAI for 0.7 s + O<sub>2</sub> plasma). The films of InO<sub>x</sub>, IAO-1, and IAO-2 were deposited to a thickness of 13 nm. The atomic percentages of the components of the IAO layers are summarized in Table 2. As shown in Figure 4a, the Al 2p peak intensities gradually increased from InO<sub>x</sub> to IAO-2 film at 73.8 eV, indicating the doping of Al atoms into the  $\text{In}^{3+}$  of  $\text{In}_2\text{O}_3$ . The Al atoms of IAO-1 and IAO-2 were doped with 1.1 and 3.8 atomic %, respectively. The Al composition increased with a decreased dose time of the indium precursor. In addition, the IAO films also contained a few atomic % of silicon oxide (Figure S6, Supporting Information). The incorporation of Si atoms in InO<sub>x</sub> is also

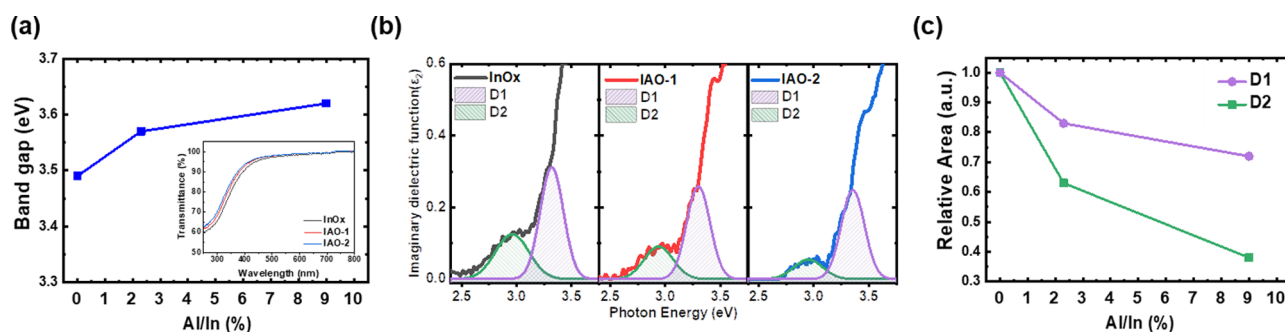


**Figure 5.** (a) Data for optical band gap of the films extracted by a Tauc plot (inset: UV–vis–NIR transmittance spectra); (b) imaginary part of the dielectric function spectra of the films with IAO/Si substrate using SE; and (c) relative area of the defects as a function of Al content.

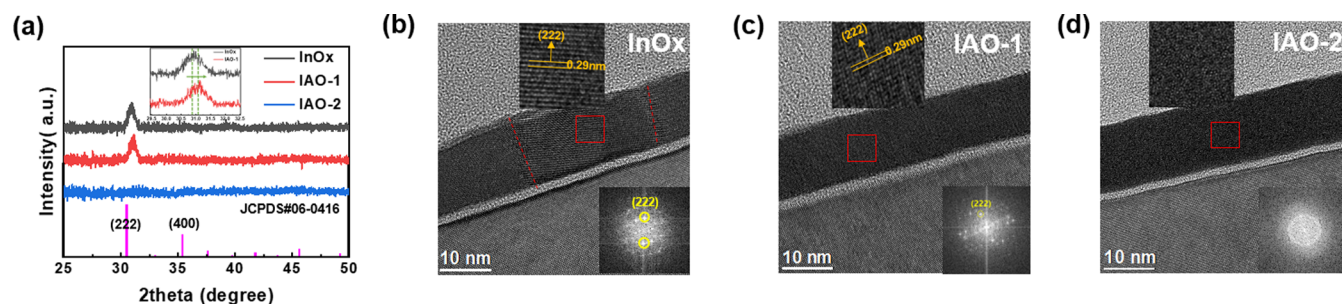


**Figure 6.** (a) XRD data of  $\text{InO}_x$  and IAO films on a glass substrate. HR-TEM images of (b)  $\text{InO}_x$  (Al/In: 0%), (c) IAO-1 (Al/In: 2%), and (d) IAO-2 (Al/In: 9%), after  $\text{O}_2$  350 °C anneal (inset: FTT of image).

known to control the carriers by suppressing the formation of oxygen vacancies.<sup>42–44</sup> The Si dopants would have originated from the fragmentation of ligand in the INCA-1 precursor, as suggested by an almost constant ratio of Si to In (Si/In) in the  $\text{InO}_x$  films regardless of the Al content. The binding energy of the In 3d peak gradually shifted to higher binding energy by adding Al, as shown in Figure 4b. Such a peak shift is associated with the oxygen binding of the corresponding metal atom.<sup>19</sup> To analyze the presence of O-related bonding, Figure 4c shows deconvolution results of O 1s peak for three Gaussian curves where the metal–oxygen (M–O) bonds, oxygen vacancies ( $\text{V}_\text{O}$ ), and hydroxyl groups (–OH) appeared at  $529.8 \pm 0.1$ ,  $530.8 \pm 0.1$ , and  $531.8 \pm 0.1$  eV, respectively. The relative areal fractions of these peaks are shown in Figure 4d. The area ratio of the M–O bonding in the IAO-1 and IAO-2 films increased with a decrease in oxygen vacancies compared with that of the  $\text{InO}_x$  thin film. While the  $\text{V}_\text{O}$  in oxide semiconductors are well known as the deep donor state, and some of them can be shallow donor, inducing carrier generation in an oxide semiconductor.<sup>45</sup> As Al atoms with a high binding energy to oxygen were added, the ratio of oxygen in the indium oxide thin film increased, thereby suppressing the carrier generation in the oxide semiconductor.

The optical transmittance of these materials was determined using UV–vis spectroscopy. All the films showed high transparency over the wavelength range of 400–900 nm, as indicated in the inset of Figure 5a. The optical band gaps of the films were extracted by the Tauc plot method, as shown in Figure 5a. The band gap increased from 3.49 to 3.62 eV with an increase in the amount of  $\text{Al}^{3+}$  dopant. As the ALD-processed  $\text{Al}_2\text{O}_3$  had a large band gap of higher than  $\sim 7$  eV, replacement of  $\text{Al}^{3+}$  into the  $\text{In}^{3+}$  sites induced an increase of band gap.<sup>46</sup> Figure 5b presents the imaginary part of the dielectric function ( $\epsilon_2$ ) spectra of the  $\text{InO}_x$  and IAO films fabricated by the PEALD process. The absorption spectrum of an oxide semiconductor film enables the characterization of its subgap states in terms of

the extinction coefficient ( $k$ ) and imaginary dielectric function ( $\epsilon_2$ ). These parameters represented the unoccupied trap state within the band gap and band edge state.<sup>47</sup> In an oxide semiconductor, these states affect the electrical properties of the semiconductor, which determine the performance of the oxide TFTs in terms of mobility and stability.<sup>48</sup> The dielectric functions ( $\epsilon = \epsilon_1 + i\epsilon_2$ ) of the  $\text{InO}_x$  and IAO films were extracted using SE. The complex refractive index ( $n$  and  $k$ ) was extracted by fitting the ellipsometry data by a fitting model. Afterward, the real and imaginary dielectric functions were calculated using the equation  $\epsilon_1 = n^2 - k^2$  and  $\epsilon_2 = 2nk$ . The origin of the subgap absorption in oxide semiconductors is related to the defects such as oxygen vacancies.<sup>49</sup> The IAO films showed a decrease in the subgap absorption compared to that of  $\text{InO}_x$ . Gaussian fitting was conducted for a detailed and quantitative analysis of the band edge state and unoccupied states near the forbidden gap.<sup>50</sup> The deconvolution of the peak consists of a shallow-level defect ( $\text{D}_1$ ) and a deep-level defect ( $\text{D}_2$ ).<sup>51,52</sup> The ionized oxygen state related to the shallow-donor was located in the  $\text{D}_1$  region, so the generation of free electrons in the IAO films was suppressed due to the decrease in the relative area of  $\text{D}_1$ . The  $\text{D}_2$  state was associated with the light instability caused by the generation of the positive charged  $\text{V}_\text{O}$ . The relative area of  $\text{D}_2$  diminished in IAO-2. This indicates that the number of trap-site decreased with the Al doping of  $\text{InO}_x$ .

The crystallinity and microstructures of  $\text{InO}_x$ , IAO-1, and IAO-2 films were examined using XRD and high-resolution transmission electron microscopy (HR-TEM) analyses. The XRD data in Figure S7a, Supporting Information, indicates that the films had an amorphous phase in the as-deposited condition. After annealing in  $\text{O}_2$  at 350 °C for 2 h (Figure 6a), the  $\text{InO}_x$  and IAO-1 thin films show a crystalline phase with XRD peaks at 30.99 and 31.17°, which is close to the (222) peaks of pure  $\text{In}_2\text{O}_3$  at approximately 30.61° (PDF#06-0416). The substitution of  $\text{Al}^{3+}$  ions into the indium in IAO-1 induced the shift of the peak

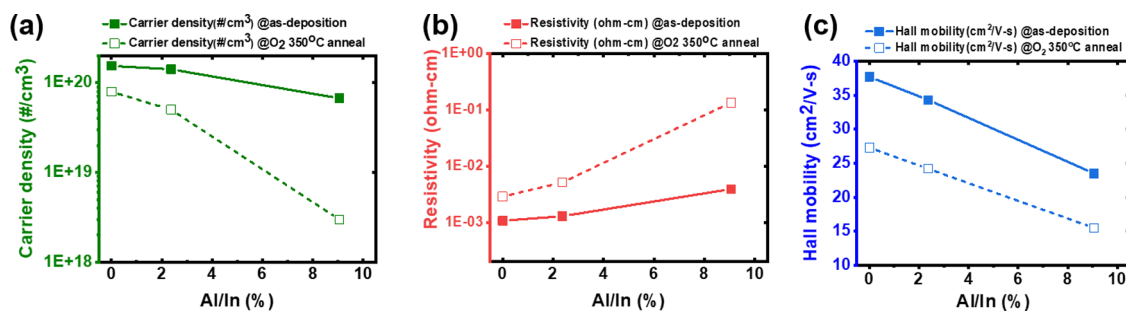


**Figure 7.** Hall measure result of InO<sub>x</sub> (Al/In: 0%), IAO-1 (Al/In: 2%) and IAO-2 (Al/In: 9%): (a) carrier density, (b) resistivity, and (c) Hall mobility (solid line: as-deposited, dash line: post-annealed).

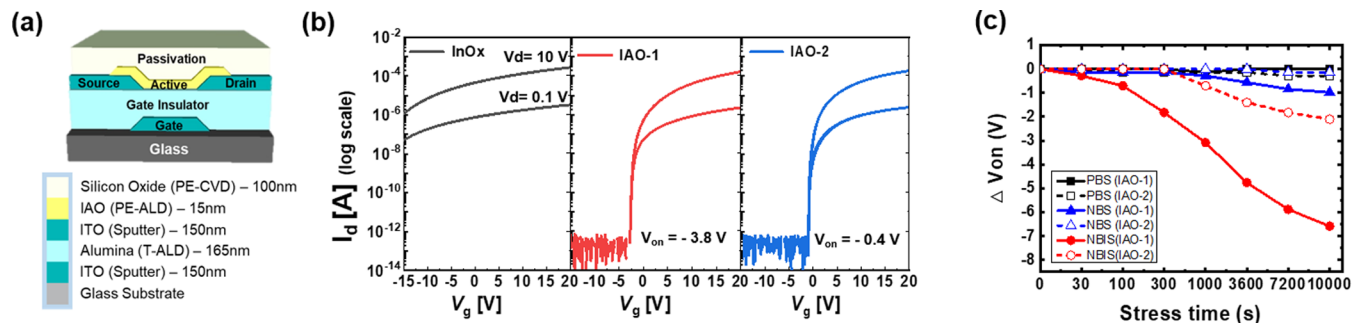


**Figure 8.** (a) TFT structure and stack material information. (b) Transfer curve of InO<sub>x</sub> TFT and IAO TFTs. (c)  $V_{on}$  shift variation during bias stability of IAO-1 TFT and IAO-2 TFT.

**Table 3. Summary of the IAO TFT Characteristics**

	SS (V/decade)	$V_{on}$ (V)	$\mu_{-}(0.1 \text{ V})$ ( $\text{cm}^2/(\text{V s})$ )	$\mu_{-}(10 \text{ V})$ ( $\text{cm}^2/(\text{V s})$ )	$N_t$ ( $10^{11} \text{ cm}^{-3}$ )
IAO-1	$0.15 \pm 0.11$	$-3.3 \pm 2.18$	$22.2 \pm 0.29$	$20.4 \pm 0.35$	2.64
IAO-2	$0.09 \pm 0.02$	$-0.4 \pm 0.35$	$18.9 \pm 0.57$	$18.4 \pm 0.57$	1.23

position of (222) to a higher diffraction angle. The positive peak shift explains that the lattice plane spacing is contracted owing to the small radius of Al<sup>3+</sup> (0.52 Å) compared to In<sup>3+</sup> (0.80 Å).<sup>18</sup> As the amount of dopant increased, the saturation of substitutional sites occurred, and then the Al atoms were located in the interstitial sites, which led to the amorphization.<sup>53</sup> Furthermore, in Figure 6b–d, HR-TEM data verified the presence of polycrystalline and amorphous phases in each sample. In the case of InO<sub>x</sub> fabricated by the PEALD process, the HR-TEM image clearly revealed a diffraction pattern with a spacing of 0.29 nm and agglomeration of the randomly oriented crystals, as shown in Figure 6b. The IAO-1 thin film doped with small Al content exhibited nanocrystallinity. The IAO-2 thin film, in which the nucleation of In<sub>2</sub>O<sub>3</sub> was suppressed by Al atoms, appeared as a homogeneous amorphous phase on the fast Fourier transform (FFT) image, as shown in Figure 6d. The elemental distribution map obtained from energy-dispersion X-ray spectroscopy (EDS) shows that Al was distributed uniformly in the IAO film, as shown in Figure S7b, Supporting Information.

Hall measurements of InO<sub>x</sub>/glass and IAO/glass samples were carried out before and after annealing under O<sub>2</sub> at 350 °C, as illustrated in Figure 7. The thermal annealing in O<sub>2</sub> atmosphere made it possible to control the carrier densities because V<sub>O</sub> were passivated by excess oxygen. Although the annealing resulted in the decrease of carrier density and Hall mobility of all films, the same trends were observed depending on the Al content. The Hall measurement displayed a decrease in carrier density from  $7.93 \times 10^{19}$  to  $2.98 \times 10^{18} \text{ cm}^{-3}$ , and an

increase in resistivity from  $2.88 \times 10^{-3}$  to  $1.35 \times 10^{-1} \Omega \text{ cm}$  by increasing the atomic percent of Al. The high binding energy of Al<sup>3+</sup> to oxygen reduces V<sub>O</sub>, thereby, the carrier density decreases.<sup>45</sup> From the XRD data after O<sub>2</sub> annealing, InO<sub>x</sub> and IAO-1 show crystalline phase which delayed the diffusion of oxygen and reduced the carrier control effect by controlling the amount of V<sub>O</sub> in the film.<sup>8</sup> Due to the intrinsic crystal structure of InO<sub>x</sub>, the influence of carrier control was reduced by corner V<sub>O</sub> sharing. The Hall mobilities were 27.3, 24.2, 15.5 cm<sup>2</sup>/(V s) in InO<sub>x</sub>, IAO-1, and IAO-2, respectively. This decrease in the Hall mobilities of the films could be attributed to their carrier concentrations.<sup>10</sup>

**Characteristics of Homogeneous IAO Thin-Film Transistors by PEALD.** We adopted the InO<sub>x</sub>, IAO-1 and IAO-2 films as the channel layer of BGBC-structured TFTs as shown in Figure 8a. The transfer curve of the optimized devices is presented in Figure 8b, and the transfer and output curves of the as-fabricated and post-annealed devices are shown in Figure S8, Supporting Information. The InO<sub>x</sub> TFTs did not show on/off characteristics both pre- and post-annealing because the large number of carriers in the InO<sub>x</sub> TFT was difficult to be fully depleted by the gate bias. Although the carrier density was reduced after heat treatment, the amount of in situ doped Si was insufficient to yield semiconducting properties of InO<sub>x</sub>. The switching characteristics of the IAO-1 TFT were shown at  $-3.3 \pm 2.18 \text{ V}$ . The IAO-2 TFT showed excellent switching performance with a turn-on voltage ( $V_{on}$ ) of  $-0.4 \pm 0.35$  pre- and post-annealing. In the case of the IAO TFT,  $V_{on}$  moved positively because the carrier concentration was reduced by

doping Al as a carrier suppressor.<sup>54</sup> Table 3 lists the electrical characteristics such as field effect mobility ( $\mu_{FE}$ ) and subthreshold swing (SS). Here,  $\mu_{FE}$  is calculated using the following equation

$$\mu_{FE} = \frac{g_m}{\frac{W}{L} \cdot C_{ox} \cdot V_d}, \quad (4)$$

where  $g_m = \partial I_d / \partial V_g$ . The gate dielectric capacitance ( $C_{ox}$ ) of the TFTs was  $4.08 \times 10^{-8}$  F/cm<sup>2</sup>. The  $\mu_{FE}$  of IAO-1 and IAO-2 is  $22.2 \pm 0.29$  and  $18.9 \pm 0.57$  cm<sup>2</sup>/(V s), respectively. The difference in mobility may be caused by a decrease in carrier densities as the Al content increased in the InO<sub>x</sub> layer. The high-current driving of IAO-2 TFTs can be observed in Figure S8b. The electrical properties were comparable to previous studies of IAO TFTs.<sup>18,54</sup> Although different TFT structures were used, ALD-IAO TFT had higher mobility and better on/off characteristics compared to ALD-InGaO TFTs with 0.74–10 cm<sup>2</sup>/(V s).<sup>21</sup>

The trap density of oxide TFT was extracted from the below equation

$$N_t = N_{bulk} + N_{it} = \frac{C_{ox}}{q} \times \left( \frac{SS \log(e)}{k_B T / q} - 1 \right), \quad (5)$$

where where  $SS = \partial \log(I_d) / \partial V_g$ ,  $q$  is the electron charge,  $k_B$  is the Boltzmann constant, and  $T$  is the absolute temperature.  $N_t$  was calculated as  $2.64 \times 10^{11}$  cm<sup>-2</sup> eV<sup>-1</sup> and  $1.23 \times 10^{11}$  cm<sup>-3</sup> eV<sup>-1</sup>, respectively, for the IAO-1 and IAO-2 TFTs. These values indicate that the number of electrons trapping states decreased with the incorporation of Al atoms, as confirmed by the XPS and SE results. The application of bias stress to the device of IAO-1 and IAO-2 TFTs was conducted at a gate bias field of  $\pm 1$  MV/cm and light power of 0.5 mW for a stress duration of 10 000 s as shown in Figure 8c. In both IAO TFTs, the  $V_{on}$  shift hardly moved under PBS. However, the IAO-1 TFT containing less Al showed a negative shift of  $-1$  V under NBS and a larger shift of approximately  $-7$  V during negative bias illumination stress (NBIS) as shown in Figure S9, Supporting Information. In contrast, the  $V_{on}$  of the IAO-2 TFT hardly moved under PBS and NBS, while under the NBIS, it shifted negatively by only  $-2$  V. The degree of NBIS stability indicates the amount of  $V_O$  located in the deep state.<sup>55,56</sup> Under illumination, the deep state of neutral  $V_O$  emitted the excess electrons to be ionized to  $V_O^{2+}$ . At the same time, the excess holes were captured by neutral  $V_O$  at the deep levels to generate ionized  $V_O^{2+}$ . In both cases, positively charged species were trapped near the interface of the active and gate insulator under negative bias to yield a negative shift of  $V_{th}$  during NBIS.<sup>56</sup> The reduction in  $V_O$  due to Al doping resulted in a small shift under NBIS. In conclusion, we obtained an IAO TFT fabricated by PEALD with good transfer characteristics and device stability under bias stress and light stress conditions.

## CONCLUSIONS

Multistep sequence ALD processes, composed of sequential dosing of INCA-1, DMAI, and oxygen plasma, in a shower head-type PEALD was applied to yield homogeneous multi-component InAlO (IAO) films. On the other hand, the TMA precursor induces etching of indium from IAO, preventing incorporation of In into the films. By adding Al, the optical bandgaps of the homogeneous IAO films were tuned between 3.49 and 3.62 eV. Decrease in the crystallinity of the IAO films was observed as the Al concentration increased. Bottom-gate

coplanar-structured TFTs were fabricated using the PEALD IAO as the channel material. The Al content in the IAO films was critical toward the electrical properties of the TFT, whose performance criteria were measured as  $V_{on}$  of  $-0.4 \pm 0.3$  V, a field effect mobility of 18.9 cm<sup>2</sup>/(V s), and subthreshold slope of 0.09 V/decade. As such, high-quality IAO films produced by PEALD may be potentially applied to the nanoelectronics and 3D-structured devices. Moreover, the control of film composition, even at the subnanometer scale, could be improved by understanding the interfacial reaction between the ALD precursors.

## ASSOCIATED CONTENT

### Supporting Information

The Supporting Information is available free of charge at <https://pubs.acs.org/doi/10.1021/acsami.1c11304>.

Summary of PEALD sequence recipe and the number of ALD cycle (Table S1); XRR data of PEALD-InO<sub>x</sub> and Al<sub>2</sub>O<sub>3</sub> films (Figure S1); XPS survey peaks and fine scan peaks of PEALD binary oxide film PEALD-Al<sub>2</sub>O<sub>3</sub> (DMAI), PEALD-Al<sub>2</sub>O<sub>3</sub> (TMA), and PEALD-In<sub>2</sub>O<sub>3</sub> (INCA-1) (Figure S2); XPS survey peaks of indium aluminum oxide films according to ALD precursor sequence: INCA-1-DMAI-O<sub>2</sub> plasma, INCA-1-TMA-O<sub>2</sub> plasma, DMAI-INCA-1-O<sub>2</sub> plasma, TMA-INCA-1-O<sub>2</sub> plasma, INCA-1-O<sub>2</sub> plasma-DMAI-O<sub>2</sub> plasma, INCA-1-O<sub>2</sub> plasma-TMA-O<sub>2</sub> plasma, DMAI-O<sub>2</sub> plasma-INCA-1-O<sub>2</sub> plasma, and TMA-O<sub>2</sub> plasma-INCA-1-O<sub>2</sub> plasma (Figure S3); summary of refractive index of indium aluminum oxide according to ALD precursor sequence (Figure S4); Frontier molecular orbitals (FMO) for In precursors and surface reaction energy of precursors on -OH surface and INCA-1 after Al precursor adsorption (Figure S5); XPS Si 2p core-level spectrum of InO<sub>x</sub>, IAO-1, and IAO-2 films (Figure S6); XRD peak of as-deposition films and EDS elemental maps of InO<sub>x</sub> (Al/In: 0%), IAO-1 (Al/In: 2%), and IAO-2 (Al/In: 9%) with In (red), Al (green), and O (blue) via HR-TEM (Figure S7); transfer curve of as-fabricated and post-annealed PEALD-InO<sub>x</sub> TFT and PEALD-IAO TFTs, and output curve of as-fabricated and post-annealed PEALD-InO<sub>x</sub> and PEALD-IAO TFTs (dot: as-fabricated, line: post-annealed) (Figure S8); and IAO TFT stability, positive bias stability (bias stress: + /cm, stress time: 10 000 s), negative bias stability (bias stress:  $-1$  MV/cm, stress time: 10 000 s), and negative illumination bias stability (bias stress:  $-1$  MV/cm, light stress: 0.5 mW, stress time: 10 000 s) (Figure S9) (PDF)

## AUTHOR INFORMATION

### Corresponding Authors

**Bonggeun Shong** – Department of Chemical Engineering, Hongik University, Seoul 04066, Republic of Korea; [orcid.org/0000-0002-5782-6300](https://orcid.org/0000-0002-5782-6300); Email: [bshong@hongik.ac.kr](mailto:bshong@hongik.ac.kr)

**Sang-Hee Ko Park** – Department of Materials Science and Engineering, Korea Advanced Institute of Science and Technology (KAIST), Daejeon 34141, Republic of Korea; [orcid.org/0000-0001-7165-8211](https://orcid.org/0000-0001-7165-8211); Email: [shkp@kaist.ac.kr](mailto:shkp@kaist.ac.kr)

## Authors

**Seunghye Lee** – Department of Materials Science and Engineering, Korea Advanced Institute of Science and Technology (KAIST), Daejeon 34141, Republic of Korea

**Miso Kim** – Department of Chemical Engineering, Hongik University, Seoul 04066, Republic of Korea

**Geumbi Mun** – Department of Materials Science and Engineering, Korea Advanced Institute of Science and Technology (KAIST), Daejeon 34141, Republic of Korea

**Jongbeom Ko** – Department of Materials Science and Engineering, Korea Advanced Institute of Science and Technology (KAIST), Daejeon 34141, Republic of Korea

**Hye-In Yeom** – Department of Materials Science and Engineering, Korea Advanced Institute of Science and Technology (KAIST), Daejeon 34141, Republic of Korea;

orcid.org/0000-0002-9370-2620

**Gwang-Heum Lee** – Department of Materials Science and Engineering, Korea Advanced Institute of Science and Technology (KAIST), Daejeon 34141, Republic of Korea

Complete contact information is available at:  
<https://pubs.acs.org/10.1021/acsami.1c11304>

## Author Contributions

S.L. and M.K. contributed equally to this work. All authors have given approval to the final version of the manuscript.

## Notes

The authors declare no competing financial interest.

## ACKNOWLEDGMENTS

This work was supported by the National Research Foundation of Korea (NRF) grant funded by the Korea government (MSIT) (2018R1A2A3075518) and “The Cross-Ministry Giga KOREA Project” grant funded by the Korea government (MSIT), (1711073921, Development of Telecommunications Terminal with Digital Holographic Table-top Display). This research was also supported by the Ministry of Trade, Industry & Energy (MOTIE; project number 20011970) and Korea Semiconductor Research Consortium (KSRC) support program for the development of the future semiconductor device, by Korea Institute for Advancement of Technology (KIAT) grant funded by the Korea Government (MOTIE)(P0012451, The Competency Development Program for Industry Specialist), and by the National Supercomputing Center with supercomputing resources including technical support (KSC-2019-CRE-0143).

## REFERENCES

- (1) Kamiya, T.; Nomura, K.; Hosono, H. Present Status of Amorphous In-Ga-Zn-O Thin-Film Transistors. *Sci. Technol. Adv. Mater.* **2010**, *11*, No. 044305.
- (2) Sheng, J.; Jeong, H.-J.; Han, K.-L.; Hong, T.; Park, J.-S. Review of Recent Advances in Flexible Oxide Semiconductor Thin-Film Transistors. *J. Inf. Disp.* **2017**, *18*, 159–172.
- (3) Cho, M. H.; Seol, H.; Song, A.; Choi, S.; Song, Y.; Yun, P. S.; Chung, K. B.; Bae, J. U.; Park, K. S.; Jeong, J. K. Comparative Study on Performance of IGZO Transistors With Sputtered and Atomic Layer Deposited Channel Layer. *IEEE Trans. Electron Devices* **2019**, *66*, 1783–1788.
- (4) Sheng, J.; Lee, H. J.; Oh, S.; Park, J. S. Flexible and High-Performance Amorphous Indium Zinc Oxide Thin-Film Transistor Using Low-Temperature Atomic Layer Deposition. *ACS Appl. Mater. Interfaces* **2016**, *8*, 33821–33828.
- (5) Lin, Y. Y.; Hsu, C. C.; Tseng, M. H.; Shyue, J. J.; Tsai, F. Y. Stable and High-Performance Flexible ZnO Thin-Film Transistors by Atomic Layer Deposition. *ACS Appl. Mater. Interfaces* **2015**, *7*, 22610–22617.

- (6) Sheng, J.; Lee, J.-H.; Choi, W.-H.; Hong, T.; Kim, M.; Park, J.-S. Review Article: Atomic Layer Deposition for Oxide Semiconductor Thin Film Transistors: Advances in Research and Development. *J. Vac. Sci. Technol., A* **2018**, *36*, No. 060801.

- (7) Luo, Y.-R. *Comprehensive Handbook of Chemical Bond Energies*; CRC Press, 2007; pp 1–1656.

- (8) Yeom, H. I.; Ko, J. B.; Mun, G.; Park, S. H. K. High Mobility Polycrystalline Indium Oxide Thin-Film Transistors by Means of Plasma-Enhanced Atomic Layer Deposition. *J. Mater. Chem. C* **2016**, *4*, 6873–6880.

- (9) Zhang, H. Z.; Cao, H. T.; Chen, A. H.; Liang, L. Y.; Liu, Z. M.; Wan, Q. Enhancement of Electrical Performance in In<sub>2</sub>O<sub>3</sub> Thin-Film Transistors by Improving the Densification and Surface Morphology of Channel Layers. *Solid-State Electron.* **2010**, *54*, 479–483.

- (10) Hosono, H. Ionic Amorphous Oxide Semiconductors: Material Design, Carrier Transport, and Device Application. *J. Non-Cryst. Solids* **2006**, *352*, 851–858.

- (11) Aikawa, S.; Nabatame, T.; Tsukagoshi, K. Effects of Dopants in InOx-Based Amorphous Oxide Semiconductors for Thin-Film Transistor Applications. *Appl. Phys. Lett.* **2013**, *103*, No. 172105.

- (12) Hennek, J. W.; Smith, J.; Yan, A.; Kim, M.-G.; Zhao, W.; Dravid, V. P.; Facchetti, A.; Marks, T. J. Oxygen “Getter” Effects on Microstructure and Carrier Transport in Low Temperature Combustion-Processed a-InXZnO (X = Ga, Sc, Y, La) Transistors. *J. Am. Chem. Soc.* **2013**, *135*, 10729–10741.

- (13) Parthiban, S.; Kwon, J. Y. Role of Dopants as a Carrier Suppressor and Strong Oxygen Binder in Amorphous Indium-Oxide-Based Field Effect Transistor. *J. Mater. Res.* **2014**, *29*, 1585–1596.

- (14) Park, J. in.; Lim, Y.; Jang, M.; Choi, S.-i.; Hwang, N.; Yi, M. Improved Stability of Aluminum Co-Sputtered Indium Zinc Oxide Thin-Film Transistor. *Mater. Res. Bull.* **2017**, *96*, 155–159.

- (15) Cho, S. H.; Ko, J. B.; Ryu, M. K.; Yang, J. H.; Yeom, H. I.; Lim, S. K.; Hwang, C. S.; Park, S. H. K. Highly Stable, High Mobility Al:SnZnInO Back-Channel Etch Thin-Film Transistor Fabricated Using PAN-Based Wet Etchant for Source and Drain Patterning. *IEEE Trans. Electron Devices* **2015**, *62*, 3653–3657.

- (16) Bak, J. Y.; Yang, S.; Yoon, S. M. Transparent Al-In-Zn-O Oxide Semiconducting Films with Various in Composition for Thin-Film Transistor Applications. *Ceram. Int.* **2013**, *39*, 2561–2566.

- (17) Fujiwara, H.; Sato, Y.; Saito, N.; Ueda, T.; Ikeda, K. Surrounding Gate Vertical-Channel FET With a Gate Length of 40 Nm Using BEOL-Compatible High-Thermal-Tolerance In-Al-Zn Oxide Channel. *IEEE Trans. Electron Devices* **2020**, *67*, 5329–5335.

- (18) Hwang, Y. H.; Jeon, J. H.; Seo, S.-J.; Bae, B.-S. Solution-Processed, High Performance Aluminum Indium Oxide Thin-Film Transistors Fabricated at Low Temperature. *Electrochem. Solid-State Lett.* **2009**, *12*, H336–H339.

- (19) Sheng, J.; Hong, T. H.; Lee, H. M.; Kim, K. R.; Sasase, M.; Kim, J.; Hosono, H.; Park, J. S. Amorphous IGZO TFT with High Mobility of 70 Cm<sup>2</sup>/(V s) via Vertical Dimension Control Using PEALD. *ACS Appl. Mater. Interfaces* **2019**, *11*, 40300–40309.

- (20) Yoon, S.-M.; Seong, N.-J.; Choi, K.; Seo, G.-H.; Shin, W.-C. Effects of Deposition Temperature on the Device Characteristics of Oxide Thin-Film Transistors Using In–Ga–Zn–O Active Channels Prepared by Atomic-Layer Deposition. *ACS Appl. Mater. Interfaces* **2017**, *9*, 22676–22684.

- (21) Sheng, J.; Park, E. J.; Shong, B.; Park, J.-S. S. Atomic Layer Deposition of an Indium Gallium Oxide Thin Film for Thin-Film Transistor Applications. *ACS Appl. Mater. Interfaces* **2017**, *9*, 23934–23940.

- (22) Baek, I.-H.; Pyeon, J. J.; Han, S. H.; Lee, G.-Y.; Choi, B. J.; Han, J. H.; Chung, T.-M.; Hwang, C. S.; Kim, S. K. High-Performance Thin-Film Transistors of Quaternary Indium–Zinc–Tin Oxide Films Grown by Atomic Layer Deposition. *ACS Appl. Mater. Interfaces* **2019**, *11*, 14892–14901.

- (23) Mackus, A. J. M.; Schneider, J. R.; Macisaac, C.; Baker, J. G.; Bent, S. F. Synthesis of Doped, Ternary, and Quaternary Materials by Atomic Layer Deposition: A Review. *Chem. Mater.* **2019**, *31*, 1142–1183.

- (24) Coll, M.; Napari, M. Atomic Layer Deposition of Functional Multicomponent Oxides. *APL Mater.* **2019**, *7*, No. 110901.
- (25) Kim, J.-H.; Ngoc Van, T. T.; Oh, J.; Bae, S.-M.; Lee, S. I.; Shong, B.; Hwang, J.-H. Plasma-Enhanced Atomic Layer Deposition of Hafnium Silicate Thin Films Using a Single Source Precursor. *Ceram. Int.* **2020**, *46*, 10121–10129.
- (26) Liu, Y. T.; Ku, C. S.; Chiu, S. J.; Lee, H. Y.; Chen, S. Y. Ultrathin Oriented BiFeO<sub>3</sub> Films from Deposition of Atomic Layers with Greatly Improved Leakage and Ferroelectric Properties. *ACS Appl. Mater. Interfaces* **2014**, *6*, 443–449.
- (27) Arroval, T.; Aarik, L.; Rammula, R.; Aarik, J. Growth of Ti<sub>x</sub>Al<sub>1-x</sub>O<sub>y</sub> Films by Atomic Layer Deposition Using Successive Supply of Metal Precursors. *Thin Solid Films* **2015**, *591*, 276–284.
- (28) Na, J. S.; Peng, Q.; Scarel, G.; Parsons, G. N. Role of Gas Doping Sequence in Surface Reactions and Dopant Incorporation during Atomic Layer Deposition of Al-Doped ZnO. *Chem. Mater.* **2009**, *21*, 5585–5593.
- (29) Elam, J. W.; George, S. M. Growth of ZnO/Al<sub>2</sub>O<sub>3</sub> Alloy Films Using Atomic Layer Deposition Techniques. *Chem. Mater.* **2003**, *15*, 1020–1028.
- (30) Zywotko, D. R.; George, S. M. Thermal Atomic Layer Etching of ZnO by a “Conversion-Etch” Mechanism Using Sequential Exposures of Hydrogen Fluoride and Trimethylaluminum. *Chem. Mater.* **2017**, *29*, 1183–1191.
- (31) Lee, Y.; Dumont, J. W.; George, S. M. Trimethylaluminum as the Metal Precursor for the Atomic Layer Etching of Al<sub>2</sub>O<sub>3</sub> Using Sequential, Self-Limiting Thermal Reactions. *Chem. Mater.* **2016**, *28*, 2994–3003.
- (32) DuMont, J. W.; Marquardt, A. E.; Cano, A. M.; George, S. M. Thermal Atomic Layer Etching of SiO<sub>2</sub> by a “Conversion-Etch” Mechanism Using Sequential Reactions of Trimethylaluminum and Hydrogen Fluoride. *ACS Appl. Mater. Interfaces* **2017**, *9*, 10296–10307.
- (33) Kim, H. G.; Kim, M.; Gu, B.; Khan, M. R.; Ko, B. G.; Yasmeen, S.; Kim, C. S.; Kwon, S.-H.; Kim, J.; Kwon, J.; Jin, K.; Cho, B.; Chun, J.-S.; Shong, B.; Lee, H.-B.-R. Effects of Al Precursors on Deposition Selectivity of Atomic Layer Deposition of Al<sub>2</sub>O<sub>3</sub> Using Ethanethiol Inhibitor. *Chem. Mater.* **2020**, *32*, 8921–8929.
- (34) Frisch, M. J.; Trucks, G. W.; Schlegel, H. B.; Scuseria, G. E.; Robb, M. A.; Cheeseman, J. R.; Scalmani, G.; Barone, V.; Petersson, G. A.; Nakatsuji, H. *Gaussian 16*; Gaussian, Inc.: Wallingford, CT, 2016.
- (35) Grimme, S.; Ehrlich, S.; Goerigk, L. Effect of the Damping Function in Dispersion Corrected Density Functional Theory. *J. Comput. Chem.* **2011**, *32*, 1456–1465.
- (36) Weigend, F.; Ahlrichs, R. Balanced Basis Sets of Split Valence, Triple Zeta Valence and Quadruple Zeta Valence Quality for H to Rn: Design and Assessment of Accuracy. *Phys. Chem. Chem. Phys.* **2005**, *7*, 3297.
- (37) Koo, J.; Kim, S.; Jeon, S.; Jeon, H.; Kim, Y.; Won, Y. Characteristics of Al<sub>2</sub>O<sub>3</sub> Thin Films Deposited Using Dimethylaluminum Isopropoxide and Trimethylaluminum Precursors by the Plasma-Enhanced Atomic-Layer Deposition Method. *J. Korean Phys. Soc.* **2006**, *48*, 131–136.
- (38) Potts, S. E.; Dingemans, G.; Lachaud, C.; Kessels, W. M. M. Plasma-Enhanced and Thermal Atomic Layer Deposition of Al<sub>2</sub>O<sub>3</sub> Using Dimethylaluminum Isopropoxide, [Al(CH<sub>3</sub>)<sub>2</sub>(μ-O<sub>i</sub>Pr)]<sub>2</sub>, as an Alternative Aluminum Precursor. *J. Vac. Sci. Technol., A* **2012**, *30*, No. 021505.
- (39) Khan, R.; Shong, B.; Ko, B. G.; Lee, J. K.; Lee, H.; Park, J. Y.; Oh, I. K.; Raya, S. S.; Hong, H. M.; Chung, K. B.; Luber, E. J.; Kim, Y. S.; Lee, C. H.; Kim, W. H.; Lee, H. B. R. Area-Selective Atomic Layer Deposition Using Si Precursors as Inhibitors. *Chem. Mater.* **2018**, *30*, 7603–7610.
- (40) Tomczak, Y.; Knapas, K.; Haukka, S.; Kemell, M.; Heikkilä, M.; Ceccato, M.; Leskelä, M.; Ritala, M. In Situ Reaction Mechanism Studies on Atomic Layer Deposition of Al<sub>x</sub>Si<sub>y</sub>O<sub>z</sub> from Trimethylaluminum, Hexakis(Ethylamino)Disilane, and Water. *Chem. Mater.* **2012**, *24*, 3859–3867.
- (41) Lee, S.; Kim, M.; Baek, G.; Kim, H.; Van, T. T. N.; Gwak, D.; Heo, K.; Shong, B.; Park, J.-S. Thermal Annealing of Molecular Layer-Deposited Indicene Toward Area-Selective Atomic Layer Deposition. *ACS Appl. Mater. Interfaces* **2020**, *12*, 43212–43221.
- (42) Mitoma, N.; Aikawa, S.; Ou-Yang, W.; Gao, X.; Kizu, T.; Lin, M. F.; Fujiwara, A.; Nabatame, T.; Tsukagoshi, K. Dopant Selection for Control of Charge Carrier Density and Mobility in Amorphous Indium Oxide Thin-Film Transistors: Comparison between Si- and W-Dopants. *Appl. Phys. Lett.* **2015**, *106*, No. 042106.
- (43) Aikawa, S.; Nabatame, T.; Tsukagoshi, K. Si-Incorporated Amorphous Indium Oxide Thin-Film Transistors. *Jpn. J. Appl. Phys.* **2019**, *58*, No. 090506.
- (44) Choi, J. Y.; Heo, K.; Cho, K.-S.; Hwang, S. W.; Chung, J.; Kim, S.; Lee, B. H.; Lee, S. Y. Effect of Si on the Energy Band Gap Modulation and Performance of Silicon Indium Zinc Oxide Thin-Film Transistors. *Sci. Rep.* **2017**, *7*, No. 15392.
- (45) Tomita, T.; Yamashita, K.; Hayafuji, Y.; Adachi, H. The Origin of N-Type Conductivity in Undoped In<sub>2</sub>O<sub>3</sub>. *Appl. Phys. Lett.* **2005**, *87*, No. 051911.
- (46) Jeon, J. H.; Hwang, Y. H.; Bae, B. S.; Kwon, H. L.; Kang, H. J. Addition of Aluminum to Solution Processed Conductive Indium Tin Oxide Thin Film for an Oxide Thin Film Transistor. *Appl. Phys. Lett.* **2010**, *96*, No. 212109.
- (47) Park, H. W.; Kwon, S.; Song, A.; Choi, D.; Chung, K. B. Dynamics of Bias Instability in the Tungsten-Indium-Zinc Oxide Thin Film Transistor. *J. Mater. Chem. C* **2019**, *7*, 1006–1013.
- (48) Kamiya, T.; Hosono, H. Material Characteristics and Applications of Transparent Amorphous Oxide Semiconductors. *NPG Asia Mater.* **2010**, *2*, 15–22.
- (49) Seo, H.; Park, C.-J.; Cho, Y.-J.; Kim, Y.-B.; Choi, D.-K. Correlation of Band Edge Native Defect State Evolution to Bulk Mobility Changes in ZnO Thin Films. *Appl. Phys. Lett.* **2010**, *96*, No. 232101.
- (50) Park, H. W.; Park, J. S.; Lee, J. H.; Chung, K. B. Thermal Evolution of Band Edge States in ZnO Film as a Function of Annealing Ambient Atmosphere. *Electrochem. Solid-State Lett.* **2012**, *15*, H133–H136.
- (51) Yoon, S.; Tak, Y. J.; Yoon, D. H.; Choi, U. H.; Park, J.-S.; Ahn, B. D.; Kim, H. J. Study of Nitrogen High-Pressure Annealing on InGaZnO Thin-Film Transistors. *ACS Appl. Mater. Interfaces* **2014**, *6*, 13496–13501.
- (52) Tak, Y. J.; Hilt, F.; Keene, S.; Kim, W. G.; Dauskardt, R. H.; Salleo, A.; Kim, H. J. High-Throughput Open-Air Plasma Activation of Metal-Oxide Thin Films with Low Thermal Budget. *ACS Appl. Mater. Interfaces* **2018**, *10*, 37223–37232.
- (53) Nakrela, A.; Benramdane, N.; Bouzidi, A.; Kebbab, Z.; Medles, M.; Mathieu, C. Site Location of Al-Dopant in ZnO Lattice by Exploiting the Structural and Optical Characterisation of ZnO: Al Thin Films. *Results Phys.* **2016**, *6*, 133–138.
- (54) Hwang, Y. H.; Bae, B. S. Effect of Aluminum and Gallium Doping on the Performance of Solution-Processed Indium Oxide Thin-Film Transistors. *J. Disp. Technol.* **2013**, *9*, 704–709.
- (55) Kamiya, T.; Nomura, K.; Hirano, M.; Hosono, H. Electronic Structure of Oxygen Deficient Amorphous Oxide Semiconductor A-InGaZnO<sub>4-x</sub>: Optical Analyses and First-Principle Calculations. *Phys. Status Solidi C* **2008**, *5*, 3098–3100.
- (56) Oh, H.; Yoon, S.-M.; Ryu, M. K.; Hwang, C.-S.; Yang, S.; Park, S.-H. K. Photon-Accelerated Negative Bias Instability Involving Subgap States Creation in Amorphous In–Ga–Zn–O Thin Film Transistor. *Appl. Phys. Lett.* **2010**, *97*, No. 183502.